



CHORUS

This is the accepted manuscript made available via CHORUS. The article has been published as:

Interlaced coarse-graining for the dynamic cluster approximation

P. Staar, M. Jiang, U. R. Hähner, T. C. Schulthess, and T. A. Maier

Phys. Rev. B **93**, 165144 — Published 27 April 2016

DOI: [10.1103/PhysRevB.93.165144](https://doi.org/10.1103/PhysRevB.93.165144)

Interlaced coarse-graining for the dynamic cluster approximation

P. Staar

IBM Research – Zurich, CH-8803 Rüschlikon, Switzerland

M. Jiang, U.R. Hähner, and T.C.S. Schulthess

Institute for Theoretical Physics, ETH Zurich, 8093 Zurich, Switzerland

T.A. Maier

*Computer Science and Mathematics Division and Center for Nanophase Materials Sciences,
Oak Ridge National Laboratory, Oak Ridge, Tennessee 37831, USA*

(Dated: April 11, 2016)

The dynamical cluster approximation (DCA) and its DCA⁺ extension use coarse-graining of the momentum space to reduce the complexity of quantum many-body problems, thereby mapping the bulk lattice to a cluster embedded in a dynamical mean-field host. Here, we introduce a new form of an interlaced coarse-graining and compare it with the traditional coarse-graining. While it gives a more localized self-energy for a given cluster size, we show that it leads to more controlled results with weaker cluster shape and smoother cluster size dependence, which converge to the results obtained from the standard coarse-graining with increasing cluster size. Most importantly, the new coarse-graining reduces the severity of the fermionic sign problem of the underlying quantum Monte Carlo cluster solver and thus allows for calculations on larger clusters. This enables the treatment of longer-ranged correlations than those accessible with the standard coarse-graining and thus can allow for the evaluation of the exact infinite cluster size result via finite size scaling. As a demonstration, we study the hole-doped two-dimensional Hubbard model and show that the interlaced coarse-graining in combination with the extended DCA⁺ algorithm permits the determination of the superconducting T_c on cluster sizes for which the results can be fit with a Kosterlitz-Thouless scaling law.

PACS numbers:

I. INTRODUCTION

Much of the numerical work in the area of strongly correlated electron materials is based on exact calculations that determine the state of a finite size lattice and regard this state as an approximation of the thermodynamic limit. The dynamic cluster approximation (DCA)^{1,2} uses a similar philosophy, in which the bulk lattice problem is represented by a finite number of cluster degrees of freedom. But in contrast to finite size calculations, the DCA uses coarse-graining to retain information about the bulk degrees of freedom not represented on the cluster. This leads to an approximation of the thermodynamic limit, in which the bulk problem is replaced by a finite size cluster embedded in a mean-field host that is designed to represent the rest of the system. This approximation makes the problem tractable so it can be solved with exact methods such as quantum Monte Carlo³.

To setup the cluster problem, one starts by dividing the first Brillouin zone (BZ) into N_c patches, each of which is represented by a cluster momentum \mathbf{K} (see Fig. 1, top left, for an example of a 16-site cluster)². One then assumes that the self-energy is well approximated by a coarse-grained self-energy^{2,4}

$$\Sigma^{\text{DCA}}(\mathbf{k}, i\omega_n) = \sum_{\mathbf{K}} \phi_{\mathbf{K}}(\mathbf{k}) \Sigma_c(\mathbf{K}, i\omega_n). \quad (1)$$

Here, $\Sigma_c(\mathbf{K}, i\omega_n)$ is the self-energy of the N_c -site cluster and the patch function $\phi_{\mathbf{K}}(\mathbf{k}) = 1$ for \mathbf{k} inside the \mathbf{K}^{th}

patch, and 0 otherwise. One then coarse-grains the Green's function

$$\bar{G}(\mathbf{K}, i\omega_n) = \frac{N_c}{N} \sum_{\mathbf{k}} \phi_{\mathbf{K}}(\mathbf{k}) \frac{1}{i\omega_n + \mu - \varepsilon_{\mathbf{k}} - \Sigma^{\text{DCA}}(\mathbf{k}, i\omega_n)} \quad (2)$$

to set up an effective cluster problem, in which the cluster self-energy $\Sigma_c(\mathbf{K}, i\omega_n) = \Sigma_c[\mathcal{G}_0(\mathbf{K}, i\omega_n)]$ is calculated as a functional of the corresponding bare cluster propagator $\mathcal{G}_0(\mathbf{K}, i\omega_n) = [\bar{G}^{-1}(\mathbf{K}, i\omega_n) + \Sigma_c(\mathbf{K}, i\omega_n)]^{-1}$. The approximation in Eq. (1) of the lattice self-energy as a piecewise constant continuation of the cluster self-energy leads to discontinuities between the patches and in some cases to strong finite size effects, manifested as a strong dependence on the cluster shape and size⁵.

In order to weaken these effects, the DCA method was recently extended through the inclusion of a lattice self-energy with continuous momentum dependence⁵. This extended DCA⁺ algorithm is obtained by reversing Eq. (1) to give a relation

$$\Sigma_c(\mathbf{K}, i\omega_n) = \frac{N_c}{N} \sum_{\mathbf{k}} \phi_{\mathbf{K}}(\mathbf{k}) \Sigma^{\text{DCA}^+}(\mathbf{k}, i\omega_n) \quad (3)$$

between the cluster self-energy $\Sigma_c(\mathbf{K}, i\omega_n)$ and the DCA⁺ lattice self-energy $\Sigma^{\text{DCA}^+}(\mathbf{k}, i\omega_n)$. As discussed in Ref.⁵, $\Sigma^{\text{DCA}^+}(\mathbf{k}, i\omega_n)$ with continuous momentum dependence is then determined from a deconvolution of Eq. (3) after the cluster self-energy $\Sigma_c(\mathbf{K}, i\omega_n)$ is interpolated between the cluster \mathbf{K} momenta. It was

shown that the DCA⁺ algorithm reduces the cluster shape and size dependence of the DCA self-energy, and, in addition, weakens the fermion sign problem⁶ of the underlying QMC cluster solver.

One usually defines the patches as the Brillouin zones of the superlattice (see Fig. 1 left) and sets $\phi_{\mathbf{K}}(\mathbf{k}) = 1$ or 0 for \mathbf{k} inside or outside the \mathbf{K}^{th} patch, respectively². But the choice of coarse-graining patch functions $\phi_{\mathbf{K}}(\mathbf{k})$ in the DCA and DCA⁺ is not unique. In Ref.⁷, for example, Gull *et al.* used a star-like patch geometry for a 4-site cluster to deform the central patch in order to capture an important part of the Fermi surface. As we will discuss, there is a set of constraints that must be satisfied by the patching. But these constraints leave ample freedom in choosing different shapes of the coarse-graining patches and different forms of the functions $\phi_{\mathbf{K}}(\mathbf{k})$.

Here, we introduce a new interlaced coarse-graining, study its effects on the self-energy of a single-band Hubbard model and compare the results with the standard coarse-graining. For small cluster sizes, we find that the interlaced coarse-graining leads to a more localized self-energy with less dependence on the shape of the cluster. In the infinite cluster size limit, it gives results that converge with those obtained from the standard coarse-graining. As an important benefit, it significantly reduces the QMC fermion sign problem, enabling calculations with larger cluster sizes. As an example, we show results for the superconducting transition temperature, for which the interlaced coarse-graining provides access to large enough clusters, so that T_c can be converged.

II. INTERLACED COARSE-GRAINING

As noted, the patching must satisfy a number of constraints⁸. First, all patches must have equal size. This ensures that the algebra of the operators of the effective cluster model obey the usual fermionic algebra. Second, the patch functions should satisfy an orthonormality condition, i.e. $\frac{N_c}{N} \sum_{\mathbf{k}} \phi_{\mathbf{K}}(\mathbf{k}) \phi_{\mathbf{K}'}(\mathbf{k}) = \delta_{\mathbf{K}\mathbf{K}'}$, so that different patches do not overlap or, in other words, at any momentum \mathbf{k} , there is exactly one \mathbf{K} for which $\phi_{\mathbf{K}}(\mathbf{k})$ is nonzero. Finally, the patches should have the same symmetry as the cluster, so that the coarse-grained Green's function and self-energy have the same symmetry as the cluster.

For the regular 4×4 cluster labeled as 16A, the standard choice of the coarse-graining patches, which we label $\phi^{(0)}(\mathbf{k})$, is shown in Fig. 1 in the top left panel. In the top right panel, we introduce a new striped coarse-graining scheme defined by the patch functions $\phi_{\mathbf{K}}^{(2)}(\mathbf{k})$, in which patches from neighboring \mathbf{K} -points are interleaved. The generation of these patches is detailed in the Appendix and the label (2) indicates the number of stripes (see Appendix). Obviously, these patches satisfy the constraints of equal volume, orthonormality and symmetry. The bottom panels show the standard

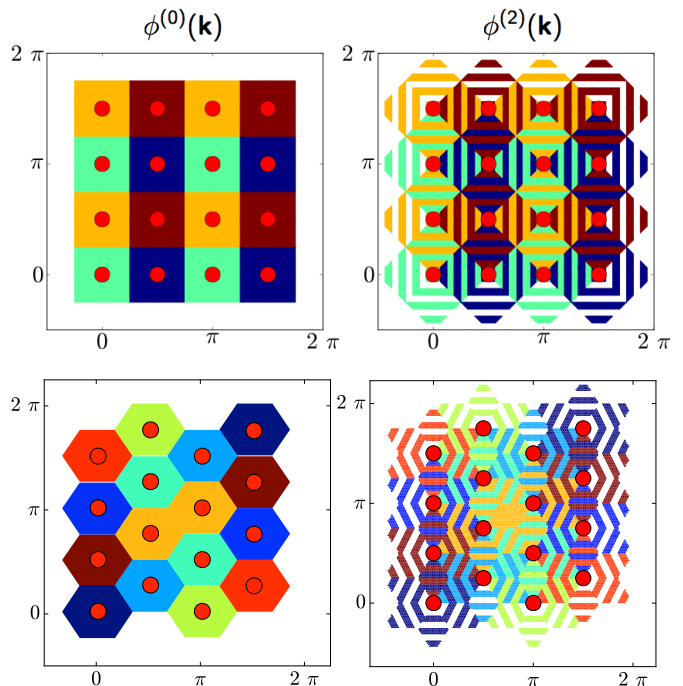


FIG. 1: The location of the cluster momenta \mathbf{K} and the shape of the patches for a 16A cluster (top) and 16B cluster (bottom). The standard coarse-graining uses the Brillouin zone of the superlattice as the patches (left), while the new coarse-graining uses patches, in which regions assigned to neighboring \mathbf{K} points are interleaved.

coarse-graining $\phi^{(0)}$ and new patching $\phi^{(2)}$ for the case of another 16-site cluster with different shape, the 16B cluster.

As discussed in Ref. [5], Eq. (2) may be interpreted as a convolution of the lattice Green's function $G(\mathbf{k}, i\omega_n)$ with the patch function $\phi_{\mathbf{K}}(\mathbf{k})$, which may also be written as $\phi(\mathbf{k} - \mathbf{K})$. Thus, the patch function essentially acts as a filter. Since it is used to map the lattice problem onto the cluster problem, it should pass the contribution to $G(\mathbf{k}, i\omega_n)$ that is localized on the cluster, and cut off contributions outside the cluster. Therefore, it is useful to investigate the coarse-graining in real space, where, after Fourier-transforming Eq. (2), one has

$$\bar{G}(\mathbf{X}, i\omega_n) = \sum_{\mathbf{x}} \phi(\mathbf{X} + \mathbf{x}) G(\mathbf{X} + \mathbf{x}, i\omega_n). \quad (4)$$

Here, a vector $\mathbf{r} = \mathbf{X} + \mathbf{x}$ to a site in the real space bulk lattice is broken up into a vector \mathbf{X} within the real space cluster and a vector \mathbf{x} to the location of a cluster in the bulk lattice, and $\phi(\mathbf{X} + \mathbf{x})$ is the Fourier-transform to real space of the patch function $\phi(\mathbf{k})$. As noted by Hettler *et al.*⁸, for a square cluster of size $L \times L$, one has for the standard coarse-graining

$$\phi^{(0)}(\mathbf{r} = \mathbf{X} + \mathbf{x}) = \prod_{l=1}^2 \left[\frac{\sin[\pi(x_l + X_l)/L]}{\pi(x_l + X_l)/L} \right], \quad (5)$$

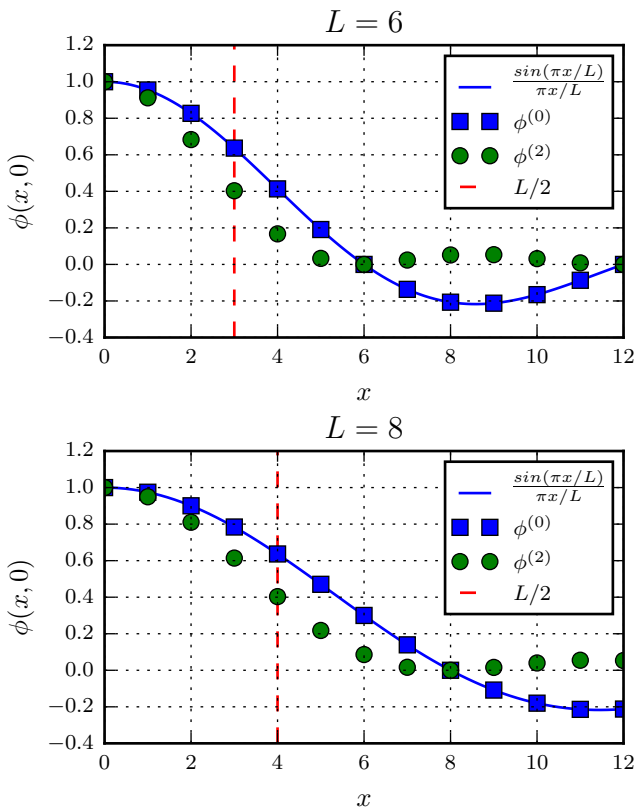


FIG. 2: (Color online) Fourier-transform of the patch functions $\phi^{(0)}(\mathbf{k})$ and $\phi^{(2)}(\mathbf{k})$ to real space for $L \times L$ clusters with $L = 6$ (top) and $L = 8$ (bottom) plotted versus $\mathbf{r} = (r, 0)$. $\phi^{(2)}(r)$ falls off more rapidly with r than $\phi^{(0)}(r)$ and remains close to 0 for $r \geq L$.

where x_l (X_l) is the l^{th} component of the vector \mathbf{x} (\mathbf{X}). Fig. 2 shows the \mathbf{r} dependence of $\phi^{(0)}(\mathbf{r})$ along the \mathbf{x} -direction $\mathbf{r} = (r, 0)$ for an $L \times L$ cluster with $L = 6$ (top) and 8 (bottom). The sinusoidal dependence of $\phi^{(0)}(\mathbf{r})$ with the $1/r$ envelope from Eq. (5) can be seen. In the same figures, we also plot the r -dependence of the new interlaced patch function $\phi^{(2)}(\mathbf{r})$. One sees that $\phi^{(2)}(\mathbf{r})$ falls off more rapidly with r than the standard patch function $\phi^{(0)}(\mathbf{r})$. This may be understood from the fact that the $\phi^{(2)}$ coarse-graining averages over a more extended momentum region and thus leads to a more local result. In addition, for distances $r > L$, $\phi^{(2)}(r)$ stays close to 0, while $\phi^{(0)}(r)$ gives a significant negative contribution to the coarse-grained average. When the lattice Green's function $G(\mathbf{r})$ is short-ranged and drops to zero for $r \geq L/2$, only the $\mathbf{x} = 0$ term contributes to $\tilde{G}(\mathbf{X})$ in the coarse-graining sum in Eq. (4), and hence $\tilde{G}(\mathbf{X}) = \phi(\mathbf{X})G(\mathbf{X})$. In this case, the standard $\phi^{(0)}$ coarse-graining gives a better approximation, since $\phi^{(0)}(r)$ is closer to 1 for $r \leq L/2$ and thus gives a $\tilde{G}(r)$ that is closer to the “real” $G(r)$. When $G(r)$ is longer-ranged, however, the $\phi^{(0)}$ coarse-graining is less controlled, since longer-ranged contributions from

neighboring clusters can contribute with either positive or negative weights, depending on the range r . This can even lead to an overestimation of the short-range correlations within the cluster. The $\phi^{(2)}$ coarse-graining, on the other hand, is always likely to underestimate the non-local correlations and thus is more controlled. As the cluster size increases, both approaches will give the same $\tilde{G}(r)$ once $L/2$ is sufficiently large relative to the length-scale over which $G(r)$ vanishes.

III. APPLICATION TO THE 2D HUBBARD MODEL

Next we study the effects of these differences in the coarse-graining on the momentum dependence of the self-energy. The Hubbard model that we study has a nearest neighbor hopping t , a next-nearest neighbor hopping t' and a Coulomb repulsion U , and its Hamiltonian is

$$H = \sum_{ij,\sigma} t_{ij} c_{i\sigma}^\dagger c_{j\sigma} + U \sum_i n_{i\uparrow} n_{i\downarrow}. \quad (6)$$

Here, $c_{i\sigma}^{(\dagger)}$ (creates) destroys an electron with spin σ on site i and $n_{i\sigma} = c_{i\sigma}^\dagger c_{i\sigma}$ is the corresponding number operator. To solve the effective cluster problem in the DCA and DCA⁺, we use the continuous-time auxiliary-field QMC algorithm developed by Gull *et al.*⁹ with high-efficiency updates¹⁰.

The top panel of Fig. 3 shows DCA results for the imaginary part of the self-energy, $\text{Im} \Sigma(\mathbf{K}, i\omega_n)$, for $\mathbf{K} = (\pi, 0)$ and $(\pi/2, \pi/2)$ obtained for the 16A cluster. Here, we have set $t' = -0.15t$, $U = 7t$ and the site filling $\langle n \rangle = 0.942$ and temperature $T = 0.125t$. For the standard coarse-graining $\phi^{(0)}$, one observes a large difference in the low frequency behavior of $\text{Im} \Sigma(\mathbf{K}, i\omega_n)$ between $\mathbf{K} = (\pi, 0)$ and $(\pi/2, \pi/2)$, which has been observed in earlier DCA calculations (see e.g. the work in Ref.⁷). The interlaced $\phi^{(2)}$ coarse-graining, in contrast, gives a self-energy with much less momentum dependence. As expected from the plots in Fig. 2 and their discussion, the $\phi^{(2)}$ patching gives a more local coarse-grained Green's function $\tilde{G}(r)$ and thus a more local self-energy $\Sigma_c[\tilde{G}]$ with less momentum dependence.

The bottom panel of Fig. 3 shows results for $\text{Im} \Sigma(\mathbf{K}, i\omega_n)$ with $\mathbf{K} = (\pi, 0)$ for both the 16A and the 16B clusters. Even though these clusters have the same size, the standard $\phi^{(0)}$ coarse-graining gives results that vary significantly between the two clusters, with qualitatively different behavior in the low frequency region. In contrast, the $\phi^{(2)}$ coarse-graining gives almost identical results for these two cluster shapes. Again, this can be understood from the fact that the interlaced $\phi^{(2)}$ coarse-graining gives a more local self-energy with weaker \mathbf{k} dependence, which thus is less affected by the location and shape of the coarse-graining patches.

As noted, one expects that this difference in the results from different forms of the coarse-graining will decrease

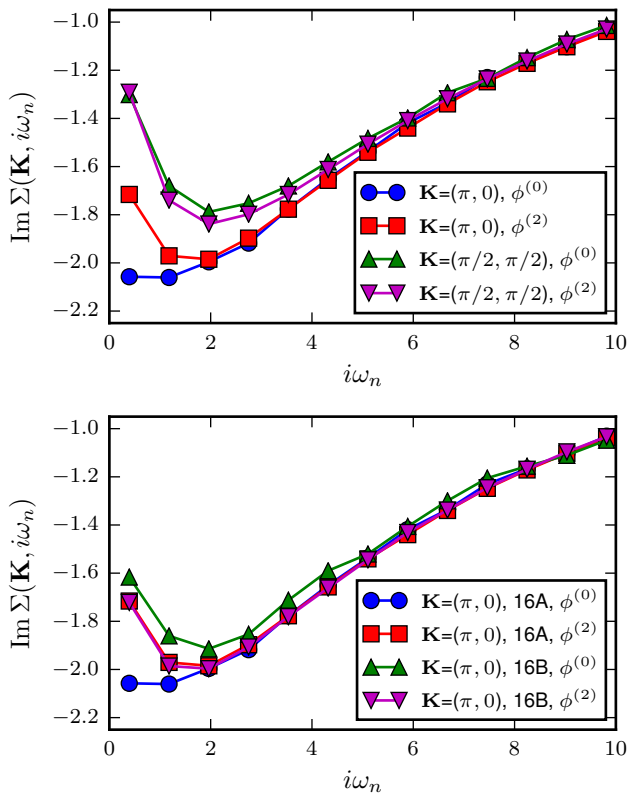


FIG. 3: (Color online) Imaginary part of the DCA self-energy for different patching $\phi^{(0)}$ and $\phi^{(2)}$ for (a) the 16A cluster for $\mathbf{K} = (\pi, 0)$ and $(\pi/2, \pi/2)$ and (b) the 16A and 16B clusters for $\mathbf{K} = (\pi, 0)$. The parameters are $t' = -0.15t$, $U = 7t$, $\langle n \rangle = 0.942$ and $T = 0.125$.

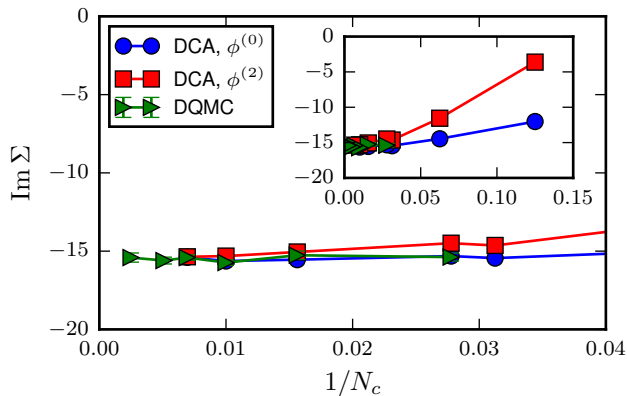


FIG. 4: (Color online) Imaginary part of the self-energy for $\mathbf{K} = (\pi, 0)$ and $\omega_0 = \pi T$ at half-filling $\langle n \rangle = 1$, $U = 8t$, $T = 0.15t$ versus the inverse cluster size $1/N_c$ obtained with DCA and $\phi^{(0)}$ (blue) and $\phi^{(2)}$ (red) coarse-graining and with determinantal QMC calculations of a finite size lattice (green). With increasing cluster size, the results obtained from the standard $\phi^{(0)}$ and the interlaced $\phi^{(2)}$ coarse-graining converge to the same large cluster DQMC result.

with increasing cluster size. To show this, we plot in Fig. 4 $\text{Im } \Sigma(\mathbf{K}, \pi T)$ with $\mathbf{K} = (\pi, 0)$ for the half-filled $\langle n \rangle = 1$ model with $t' = 0$ and $U = 8t$ for the $\phi^{(0)}$ and $\phi^{(2)}$ patching. Also shown in this figure are large cluster results obtained on a finite size lattice with the determinantal QMC (DQMC) algorithm¹¹. One sees that for small cluster sizes, the standard $\phi^{(0)}$ coarse-graining gives much better results that converge faster to the exact large N_c limit, while the $\phi^{(2)}$ coarse-graining underestimates the correlations. Again, this is expected from the differences in real space r behavior of the $\phi^{(0)}(r)$ and $\phi^{(2)}(r)$ shown in Fig. 2. With increasing cluster size, however, both curves converge to the same large cluster DQMC result.

Next we turn to the effects of the coarse-graining on the fermion sign problem of the underlying QMC solver. For the doped $\langle n \rangle \neq 1$ Hubbard model in Eq. (6), the sign problem is found to become exponentially worse with increasing lattice size, decreasing temperature and increasing U ¹². QMC simulations of the doped model are therefore limited to small lattices, high temperatures or weak coupling U . QMC simulations within the framework of the DCA^{1,2,8} have been found to have a much less severe sign problem than QMC simulations of finite size lattices³. Lacking a rigorous mathematical argument, the DCA improvement of the sign problem was attributed to the action of the mean-field host on the cluster³. This has allowed QMC calculations at lower temperatures and larger U than those accessible by finite size QMC simulations². Further progress was made with the introduction of the DCA⁺ method⁵, which was found to exhibit an additional reduction of the sign problem. This was ascribed to the removal of artificial long-range correlations, which arise in the DCA because of the discontinuities in the self-energy, through a continuous lattice self-energy in the DCA⁺⁵.

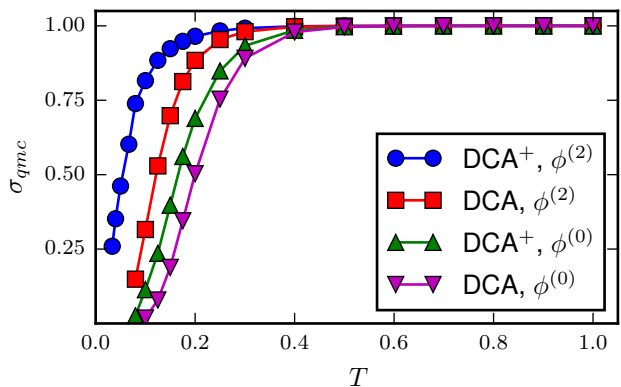


FIG. 5: The average QMC sign versus temperature for $U/t = 8$ and $\langle n \rangle = 0.9$ for the 16A cluster. The use of the DCA⁺ and the $\phi^{(2)}$ patching lead to a significantly larger average sign.

Here we study the effect of the coarse-graining on the sign problem. Fig. 5 shows the temperature dependence

of the average QMC sign for the 16A cluster with $t' = 0$, $U = 8t$ and $\langle n \rangle = 0.9$ for both DCA and DCA⁺ calculations with $\phi^{(0)}$ and $\phi^{(2)}$ coarse-graining. At low temperatures, one sees that the QMC sign falls rapidly to zero, and as noted, the DCA⁺ algorithm gives an improved sign relative to the DCA algorithm. As one sees, a significant further improvement is achieved with the interlaced $\phi^{(2)}$ coarse-graining. When combined with the DCA⁺ algorithm, it has a significantly larger average sign at low temperatures than the DCA algorithm with standard $\phi^{(0)}$ patching. For example, at $T = 0.2t$, the sign in the DCA/ $\phi^{(0)}$ calculation has fallen to 0.5, while the sign in the DCA⁺/ $\phi^{(2)}$ calculation remains almost 1. As a consequence, one sees that the DCA⁺/ $\phi^{(2)}$ combination enables calculations with a sizeable sign at much lower temperatures than those that are accessible with just the DCA or the standard coarse-graining.

Finally, we illustrate the benefits of the improved sign problem by calculating the superconducting transition temperature T_c as a function of cluster size N_c . To calculate T_c , we determine the eigenvalues λ_α and eigenvectors $\phi_\alpha(k)$ of the Bethe-Salpeter equation¹³

$$-\frac{T}{N} \sum_k \Gamma^{pp}(k, k') G(k') G(-k') \phi_\alpha(k') = \lambda_\alpha \phi_\alpha(k), \quad (7)$$

where $k = (\mathbf{k}, i\omega_n)$ and $\Gamma^{pp}(k, k')$ is the irreducible particle-particle vertex on the bulk lattice. In the DCA⁺, just as the self-energy in Eq. (3), the lattice vertex $\Gamma^{pp}(k, k')$ is determined from inverting the equation

$$\Gamma_c^{pp}(K, K') = \frac{N_c^2}{N^2} \sum_{\mathbf{K}, \mathbf{K}'} \phi_{\mathbf{K}}(\mathbf{k}) \Gamma^{pp}(k, k') \phi_{\mathbf{K}'}(\mathbf{k}') \quad (8)$$

as described in Ref.¹⁴. At T_c , the leading eigenvalue crosses 1 and one finds that the corresponding eigenvector has $d_{x^2-y^2}$ symmetry¹⁴.

In Fig. 6, we plot $T_c(N_c)$ for $U = 4t$, $t' = 0$ and $\langle n \rangle = 0.9$ from DCA⁺ calculations with the standard $\phi^{(0)}$ and the new interlaced $\phi^{(2)}$ coarse-graining. In the region with $N_c \leq 32$ the trends are clearly different: The $\phi^{(0)}$ coarse-graining gives a T_c that decreases with N_c and thus apparently overestimates the pairing correlations in small clusters, while the $\phi^{(2)}$ coarse-graining gives an increasing $T_c(N_c)$. This increase can again be traced to the stronger locality of the $\phi^{(2)}$ coarse-graining. The d -wave pairing strength arises from a pairing interaction $\Gamma^{pp}(k, k')$ that increases with momentum transfer $\mathbf{k} - \mathbf{k}'$ ¹³. In small clusters, the $\phi^{(2)}$ coarse-graining underestimates this momentum dependence and thus T_c . With increasing cluster size, this underestimation is reduced, and T_c increases with N_c . For $N_c = 32$, both approaches give similar T_c . While the sign problem of the standard coarse-graining prevents calculations for $N_c > 32$, the interlaced coarse-graining allows simulations of significantly larger clusters. As one sees from Fig. 2, the $\phi^{(2)}$ coarse-graining takes into account correlations in these larger clusters which

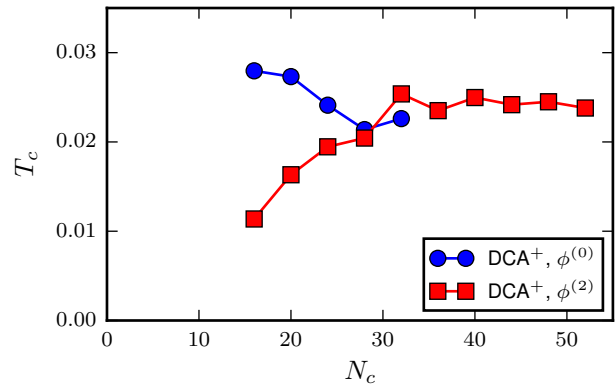


FIG. 6: (Color online) d -wave superconducting transition temperature T_c versus cluster size from DCA⁺ calculations with the interlaced $\phi^{(2)}$ and standard $\phi^{(0)}$ coarse-graining for $U = 4t$, $t' = 0$ and $\langle n \rangle = 0.9$. The improved sign problem of the $\phi^{(2)}$ coarse-graining algorithm enables calculations on much larger clusters, for which the results converge to the asymptotic large cluster limit.

are longer-ranged than those taken into account by the $\phi^{(0)}$ coarse-graining in the smaller clusters. This is particularly useful for the study of phase transitions where the critical behavior is determined by the long-range correlations. One sees that the $\phi^{(2)}$ coarse-graining gives results with smooth cluster size dependence in the $N_c \geq 32$ region, which is not accessible by the standard $\phi^{(0)}$ coarse-graining. As previously discussed in Ref.¹⁴, the clusters in this region are large enough so that the results are consistent with the asymptotic Kosterlitz-Thouless scaling behavior that is expected to describe the superconducting transition in a 2D system. From this, one can determine T_c for the exact infinite cluster size limit, as shown in Ref.¹⁴.

IV. SUMMARY AND CONCLUSIONS

To conclude, we have introduced and studied a new form of an interlaced coarse-graining for the DCA and DCA⁺ algorithms to map the bulk lattice to an effective cluster problem and compared it with the standard coarse-graining. This interlaced coarse-graining averages over a more extended region in momentum space and thus gives a more localized self-energy with weaker k -dependence. Non-local correlations are thus potentially underestimated in small clusters and, in the absence of the QMC sign problem, the standard coarse-graining converges faster to the exact infinite cluster size result. However, the interlaced coarse-graining generally gives more controlled results with weaker cluster shape and smoother cluster size dependence that converge with the results from the standard coarse-graining with increasing cluster size. Most importantly, we find that the interlaced coarse-graining significantly reduces the

sign problem of the underlying QMC solver, thereby enabling calculations with larger cluster sizes, for which longer-ranged correlations are taken into account and the underestimation of shorter-ranged correlations is not an issue. The new coarse-graining is thus particularly well suited for large cluster studies of phase transitions where the critical behavior is determined by the long-range correlations. We should note that pushing the interlaced coarse-graining further by averaging over an even larger momentum region will suppress non-local correlations even more, which eventually will have a detrimental effect since larger cluster sizes will be needed for convergence. It is therefore important to find a good balance between the benefits of an improved sign problem and the undesirable effect of suppressing the non-local correlations. As an example, we have shown that the interlaced coarse-graining in combination with the DCA⁺ algorithm enables calculations of the superconducting T_c on cluster sizes, for which the results converge to the asymptotic Kosterlitz-Thouless scaling curve. Thus, while care should be taken in interpreting results on small clusters, the new coarse-graining introduced in this paper gives access to much larger cluster sizes and thus can enable a finite size scaling analysis to recover the exact infinite cluster size result.

Acknowledgments

We would like to thank Richard Scalettar for useful comments. Part of this research was conducted at the Center for Nanophase Materials Sciences, which is a DOE Office of Science User Facility. An award of computer time was provided by the Innovative and Novel Computational Impact on Theory and Experiment (INCITE) program. This research used resources of the Oak Ridge Leadership Computing Facility, which is a DOE Office of Science User Facility supported under Contract DE-AC05-00OR22725.

Appendix: Setup of interlaced coarse-graining patches

In this section we describe the algorithm that generates the interlaced coarse-graining patches for the two dimensional case. We start from the traditional coarse-graining patches defined as the Brillouin zones of the superlattice. We call the edges and corners of these patches *facets* and *simplexes*, respectively. First, each initial patch is divided into triangles by connecting the corners of the patch with its center, i.e. the cluster momentum \mathbf{K} . For example, the square shaped initial patches of the 16A cluster are split into four triangles while the hexagonal shaped initial patches of the 16B cluster are divided into six triangles. Each of these triangles has a unique facet as one edge. The vector perpendicular to the facet that connects the center to the

facet is defined as the normal vector \mathbf{n} of the triangle. We then recursively subdivide each triangle into four similar triangles by connecting the midpoints of each side. By construction, this *k-mesh refinement* at the same time divides the initial triangle into stripes of equal width parallel to its facet (see Fig. 7). The details of the first three recursion steps are listed in Tab. I for the 16B cluster.

recursion	0	1	2	3	k
no. triangles	6	24	96	384	6×4^k
no. stripes	1	2	4	8	2^k
max. no. periods	0	1	2	4	2^{k-1}

TABLE I: Details of the k-mesh refinement for the 16B cluster up to three recursion steps. The initial number of triangles for the hexagonal shaped patch is six. Each recursion step divides the triangles into four similar, smaller triangles. The number of stripes is doubled each time. The maximum number of periods is the number of stripes divided by two.

For each of the smallest triangles we compute the center of mass \mathbf{k}_{cm} and project it onto the normal vector \mathbf{n} of its initial triangle. The interlaced patches of *period* p are then obtained by reflecting those triangles across the facet for which

$$\sin\left(\frac{2\pi p}{\mathbf{n} \cdot \mathbf{n}} \mathbf{k}_{\text{cm}} \cdot \mathbf{n}\right) < 0. \quad (\text{A.1})$$

For the 16B cluster this is illustrated in Fig. 7 for one period (blue-yellow) and three periods (blue-green). First note that by construction stripes always get reflected as a whole. As its name indicates, p is just the number of periods of the sine along the normal vector \mathbf{n} . For the stripes not to cross a node of the sine, their total number in the initial triangle should be an even multiple of the number of periods p . Consequently, p determines the minimum number of recursion steps required.

One advantage of this new approach of generating the coarse-graining patches is its recursive nature. The larger the recursion depth, the more the patches become interlaced. But at the same time the only geometric structures occurring are triangles, which are easy to integrate over. The traditional coarse-graining is a special case and corresponds to zero recursion steps. Last but not least, this new coarse-graining approach can easily be generalized to three dimensions, in which triangles become tetrahedrons.

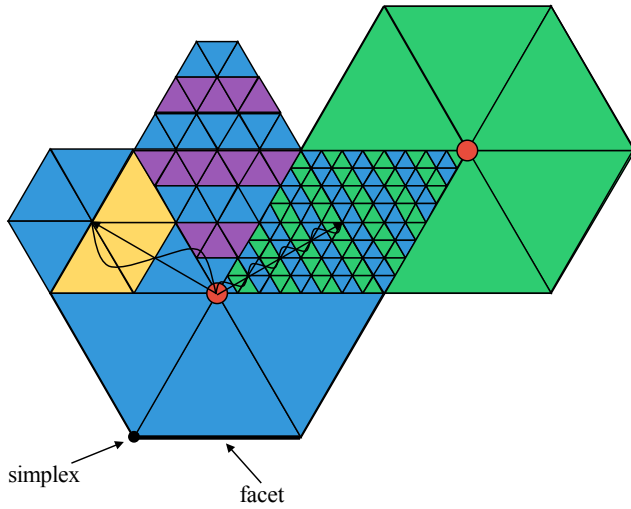


FIG. 7: (Color online) Construction of the patches for the 16B cluster. Successive recursion steps of the k -mesh refinement are shown: 0 (plain blue), 1 (blue-yellow), 2 (blue-purple) and 3 (blue-green). Stripes are reflected with the maximum number of periods possible: 0, 1, 2 and 4. The sine, that determines whether a stripe is reflected, is sketched for $p = 1$ and $p = 4$ in recursion step 1 and 3, respectively.

-
- ¹ M. H. Hettler, A. N. Tahvildar-Zadeh, M. Jarrell, T. Pruschke, and H. R. Krishnamurthy, *Physical Review B* **58**, R7475 (1998).
- ² T. Maier, M. Jarrell, T. Pruschke, and M. Hettler, *Reviews of Modern Physics* **77**, 1027 (2005).
- ³ M. Jarrell, T. Maier, C. Huscroft, and S. Moukouri, *Physical Review B* **64**, 195130 (2001).
- ⁴ S. Okamoto, A. J. Millis, H. Monien, and A. Fuhrmann, *Physical Review B* **68**, 195121 (2003).
- ⁵ P. Staar, T. Maier, and T. C. Schulthess, *Physical Review B* **88**, 115101 (2013).
- ⁶ M. Troyer and U. Wiese, *Physical Review Letters* **94**, 170201 (2005).
- ⁷ E. Gull, M. Ferrero, O. Parcollet, A. Georges, and A. Millis, *Physical Review B* **82**, 155101 (2010).
- ⁸ M. Hettler, M. Mukherjee, M. Jarrell, and H. Krishnamurthy, *Physical Review B* **61**, 12739 (2000).
- ⁹ E. Gull, P. Werner, O. Parcollet, and M. Troyer, *Europhysics Letters* **82**, 57003 (2008).
- ¹⁰ E. Gull, P. Staar, S. Fuchs, P. Nukala, M. Summers, T. Pruschke, T. Schulthess, and T. Maier, *Physical Review B* **83**, 075122 (2011).
- ¹¹ R. Blankenbecler, D. Scalapino, and R. Sugar, *Physical Review D* **24**, 2278 (1981).
- ¹² E. Y. Loh, J. E. Gubernatis, R. T. Scalettar, S. R. White, D. J. Scalapino, and R. L. Sugar, *Physical Review B* **41**, 9301 (1990).
- ¹³ T. A. Maier, M. S. Jarrell, and D. J. Scalapino, *Physical Review Letters* **96**, 047005 (2006).
- ¹⁴ P. Staar, T. Maier, and T. C. Schulthess, *Physical Review B* **89**, 195133 (2014).